Transient photoconductivity in GaAs as measured by time-resolved terahertz spectroscopy

Matthew C. Beard, Gordon M. Turner, and Charles A. Schmuttenmaer
Chemistry Department, Yale University, 225 Prospect Street, P.O. Box 208107, New Haven, Connecticut 06520-8107
(Received 6 December 1999; revised manuscript received 17 March 2000)

The onset and decay of photoconductivity in bulk GaAs has been measured with 200-fs temporal resolution using time-resolved THz spectroscopy. A low carrier density ($<2\times10^{16}$ cm^{-3}) with less than 100-meV kinetic energy was generated via photoexcitation. The conductivity was monitored in a noncontact fashion through absorption of THz (far-infrared) pulses of several hundred femtosecond duration. The complex-valued conductivity rises nonmonotonically, and displays nearly Drude-like behavior within 3 ps. The electron mobilities obtained from fitting the data to a modified Drude model (6540 cm^2 V^{-1} s^{-1} at room temperature with $N=1.6\times10^{16}$ cm^{-3}, and 13600 cm^2 V^{-1} s^{-1} at 70 K with $N=1.5\times10^{16}$ cm^{-3}) are in good agreement with literature values. There are, however, deviations from Drude-like behavior at the shortest delay times. It is shown that a scalar value for the conductivity will not suffice, and that it is necessary to determine the time-resolved, frequency-dependent conductivity. From 0 to 3 ps a shift to higher mobilities is observed as the electrons relax in the Γ valley due to LO-phonon-assisted intravalley absorption. At long delay times (5–900 ps), the carrier density decreases due to bulk and surface recombination. The time constant for the bulk recombination is 2.1 ns, and the surface recombination velocity is 8.5×10^5cm/s.

I. INTRODUCTION

Ultrafast carrier dynamics in semiconductors have been of great interest for the last few decades, and GaAs is the high-speed semiconductor of choice.[1,2] Experimental techniques of time-resolved optical transmission,[3–9] reflection, electro-optic sampling,[10,11] luminescence,[12–15] four-wave mixing,[16,17] and photon echoes,[18,19] among others, have all contributed to a more complete understanding of carrier dynamics in semiconductors. Theoretical models of carrier dynamics have ranged from coupled rate equations[20] to Monte Carlo simulations,[21–24] to semiconductor Bloch equations[25] and Boltzmann transport theory.[26,27] This paper reports on the time-resolved, frequency-dependent photoconductivity of GaAs based on measurement of the intraband absorption.

Time-resolved THz spectroscopy (TRTS) is a noncontact electrical probe capable of determining photoconductivity with a temporal resolution of better than 200 fs. Methods such as transient absorption or time-resolved luminescence, which are sensitive to either the sum or the product of the electron and hole distribution functions, respectively, do not measure the actual conductivity. Unlike luminescence, this technique is also applicable to a study of carrier dynamics in indirect-gap semiconductors. Even methods which are sensitive to the diffusion of carriers, such as transient grating or four-wave mixing, are not able to determine the frequency-dependent conductivity. The high sensitivity of TRTS makes it possible to carry out measurements with photoexcited carrier column densities as low as 5×10^{10} cm^{-2} in GaAs (equivalent to a carrier density of 5×10^{14} cm^{-3}, with a skin depth of 1 μm).

The ability to characterize electrical properties in a noncontact fashion with subpicosecond temporal resolution is necessary in the field of nanoscale electronics and optoelectronics, where it is difficult, if not impossible, to use conventional probes. Knowledge of a material's frequency-dependent conductivity is important for its use in electronic devices. Therefore, one of the motivating factors for this work was to benchmark the TRTS technique on a well-studied system before proceeding to study systems that are not as well characterized.

This study was also motivated in part by a series of papers by Vengurlekar and Jha that theoretically predicted a dramatic variation of the frequency-dependent mobility of photoexcited electrons as a function of their initial kinetic energy.[26–30] If the initial electron kinetic energy is an integral multiple of the LO-phonon energy, then tremendous variations and oscillations in the frequency-dependent conductivity are predicted during the first couple of picoseconds after photoexcitation. On the other hand, if the initial kinetic energy is a half-integral multiple of the LO-phonon energy, the onset of photoconductivity is predicted to smoothly approach Drude-like behavior. We have carried out a full time-resolved study of the relaxation dynamics that has produced results directly comparable to these theoretical predictions. While our results agree with some of the features of Vengurlekar and Jha's predictions, we do not observe differences based on whether the initial kinetic energy is integer or half-integer multiples of the LO-phonon energy.

The time-dependent conductivity is given by $\sigma(t)=en(t)\mu(t)$, where $n(t)$ is the time-dependent carrier density, $\mu(t)$ is the time-dependent mobility, and e is the electron charge. The carrier density will change on time scales of ~5 ps due to surface recombination, and ~100 ps due to bulk recombination and diffusion. Therefore, changes in $\sigma(t)$ will reflect changes in $\mu(t)$ for times interval <5 ps. The mobility is related to the dynamics of the semiconductor through both the effective mass m^* and the carrier scattering rate γ by $\mu(t)=e/[\gamma(t)m^*(t)]$. The effective mass is time dependent because the photoexcited electron distribution $f(E,t)$ is itself time dependent:

$$m^*(t)=\frac{1}{\int f(E,t)\frac{1}{\hbar^2}\frac{d^2E}{dk^2}dk}. \tag{1}$$

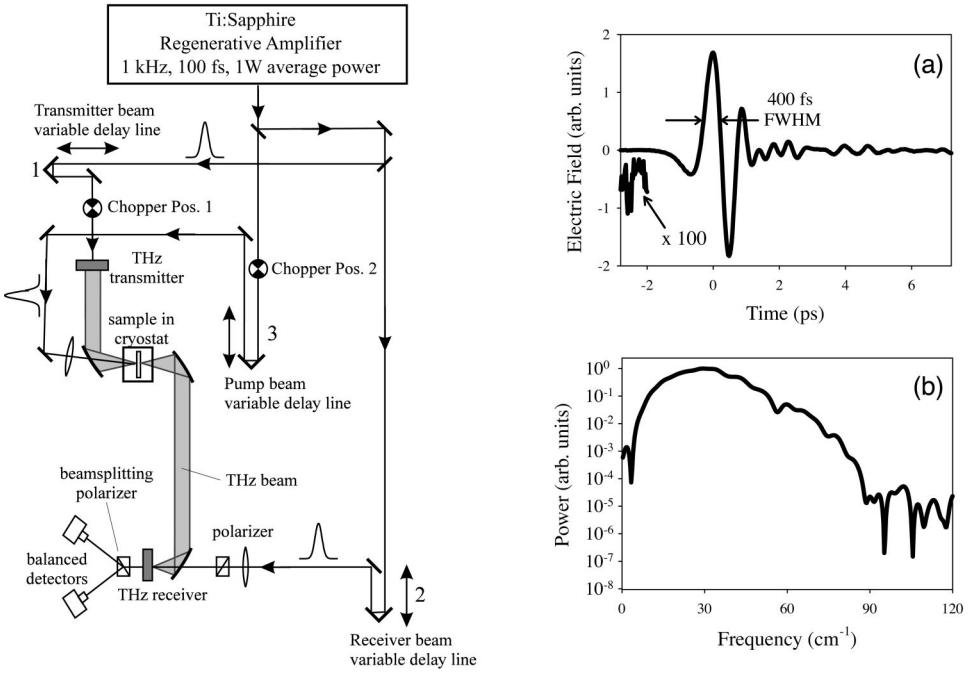

FIG. 1. Experimental apparatus used to collect TRTS spectra. A reference scan is collected with the chopper in position 1, and a photoexcited difference scan is collected with the chopper in position 2. The THz amplitude is monitored by changing the relative delay of table 1 or table 2 depending on the type of experiment being performed (see text for more detail). Delay table 3 is used to change the relative delay of the pump beam. Plot (a) shows a typical time-domain THz transient of about 400 fs duration (FWHM) and a signal-to-noise ratio of roughly 1000:1. Plot (b) shows the power spectrum of the THz pulse.

This has been observed using visible pump/THz probe experiments where the photoexcited electrons have sufficient energy to access the *X* and *L* valleys, both of which have low curvature (d^2E/dk^2) and thus low mobility.[31–33] The THz response is then dominated by the electron population scattering back to the Γ valley rather than a time-dependent scattering rate. To probe the time-dependent scattering rate independent of intervalley scattering, photoexcitation into the Γ valley with a small excess energy is required.

This work significantly extends some of the most closely related studies. Nuss and co-workers performed time-resolved electro-optic sampling measurements of GaAs, but used 2.0-eV photon energies, which allowed electrons to scatter to the low mobility satellite valleys.[31,34] A time-resolved THz transmission study of GaAs that used similar high photon energies was reported by Green *et al.*[35] A study of GaAs and InP, which also included frequency-resolved spectra 7 ps after photoexcitation, was reported by Saeta *et al.*[36] Groeneveld *et al.* measured carrier and exciton far-IR spectra at several pump-probe delay times in GaAs-$Al_xGa_{1-x}As$ quantum wells.[37] Ralph and co-workers investigated the overall change in carrier absorption as a function of time, but were only able to determine the frequency-dependent conductivity on a much longer time scale because they used bolometric detection rather than electrooptic sampling.[33,38] Flanders *et al.* reported the average change in THz transmission after photoexcitation, as well as frequency resolved absorbance spectra for five pump-probe delay times when using excitation energies low enough to prevent intervalley scattering.[39] Finally, Schall and Jepsen recently investigated the interface effects on propagation of THz pulses through photoexcited GaAs.[40] While all of these pioneering studies provided a glimpse into photoexcited carrier dynamics, none fully characterized the time-resolved, frequency-dependent photoconductivity.

II. EXPERIMENTAL METHODS

The significant developments required to extend TRTS experiments to the subpicosecond time scale are only briefly discussed in this section. Additional description of these developments can be found in Ref. 41. It is very important to stress that the data *must* be worked up correctly if meaningful results are to be obtained.

A. Experimental apparatus

The time-resolved THz spectrometer is shown schematically in Fig. 1. A Spectra Physics regenerative amplifier system (Millennia-Tsunami-Merlin-Spitfire) produces a 1-kHz pulse train of 1-mJ, 800-nm pulses of 100 fs duration [full width at half maximum (FWHM)]. This beam is split into three portions, each of which is responsible for either the THz transmitter, THz receiver, or visible photoexcitation arms of the spectrometer (labeled 1, 2, and 3 respectively). For reduced bandwidth experiments described below, the output of the laser is modified. Metal beam blocks are placed in the compressor of the amplifier to block the low- and high-frequency regions of the bandwidth of the uncompressed pulse. After recompression, the resultant pulses have a duration of approximately 280 fs (FWHM), and a reduced bandwidth of about 6 nm.

Terahertz generation occurs through nonresonant optical rectification[42,43] of the visible pulse in a 1-mm-thick $\langle 110 \rangle$ ZnTe crystal (II-IV Inc.). The THz radiation is detected by free-space electro-optic sampling[43–47] in another 0.5-mm-thick $\langle 110 \rangle$ ZnTe crystal. The signal is collected with a lock-in amplifier (Stanford Research Systems SR830) phase-locked to an optical chopper which modulates either the THz generation arm or the pump beam. We usually collect data with the chopper in the pump beam; thus, to determine the photoexcited scan, the difference scan must be added to a reference scan collected with the chopper in the probe beam.

A collimated 2-mm-diameter visible beam of 230 μJ/pulse is used for THz generation, and a focused 200-μm-diameter visible beam of 4.5 nJ/pulse is used for THz detection. For GaAs experiments, the pump beam energy is attenuated to less than 1 μJ/pulse to keep the total number of photoexcited carriers below 2×10^{16} cm^{-3}.

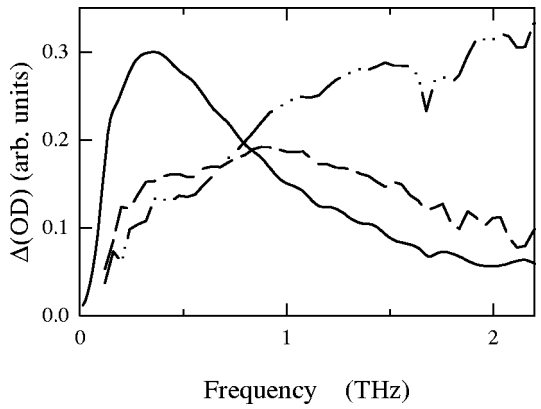

FIG. 2. Change in optical density spectra of photoexcited GaAs as a function of visible (pump) spot size at a 20-ps pump-probe delay time. The visible spot sizes are 6.0 mm (solid line), 1.7 mm (dashed line), and 1.1 mm (dot dashed line), whereas the THz spot size is 2.3 mm. The spectrum becomes skewed toward higher frequencies as the visible spot size becomes smaller than the THz spot size.

The THz beam path from the transmitter to the receiver is enclosed and purged with dry nitrogen. The sample is placed in a variable temperature cryostat (Janis model ST-100, with LakeShore model 321 temperature controller) fitted with single-crystal *z*-cut quartz windows rotated to minimize THz generation. The sample consists of a 0.46-mm-thick GaAs wafer in the $\langle 100 \rangle$ orientation to ensure that it does not generate THz radiation upon photoexcitation.[48]

We find that when the spot size (the diameter at which the intensity of a Gaussian beam falls to $1/e^2$ of its value at the beam center) of the pump is the same size as or smaller than the probe, the extracted spectrum is skewed to higher frequencies (see Fig. 2). Therefore, the spot size of the visible (pump) was at least two times larger than that of the THz (probe) beam, so that the probe beam sampled a uniform region of photoexcitation. The spot sizes were determined by comparing the beam intensities measured through a set of brass pinholes of known diameter. The visible spot size diameter was between 9 and 11 mm, and the THz spot size was typically between 3 and 5 mm. The pinholes were also used to overlap the THz and visible beams at the sample. The THz and visible beams were copropagated to minimize temporal smearing.

B. Data acquisition and analysis

Complete TRTS experiments require collecting a THz difference scan at a series of pump-probe delay times. We refer to this full data set as a two-dimensional (2D) scan. It is also possible to scan one delay line while holding the other fixed. This is referred to as a 1D scan, and can be collected as such, or obtained numerically from the 2D data. A 1D *probe* scan is obtained when the pump delay line (3) is fixed and the THz receiver delay line (2) is scanned. A 1D probe scan is only meaningful when obtaining data at least 3 ps after time zero ($t=0$). A 1D *pump* scan is obtained when the THz receiver delay line is fixed at the peak of the THz pulse and the pump delay line is scanned. A 1D pump scan provides useful information about the average THz absorption by the sample. For example, 1D pump scans of GaAs (Fig. 3) show that the carriers take longer to return to the high-mobility Γ valley (Fig. 4) as a function of increasing photoexcitation energy. This type of 1D TRTS is similar to other time-resolved pump-probe techniques where the change in transmission ($\Delta T/T$) is measured.

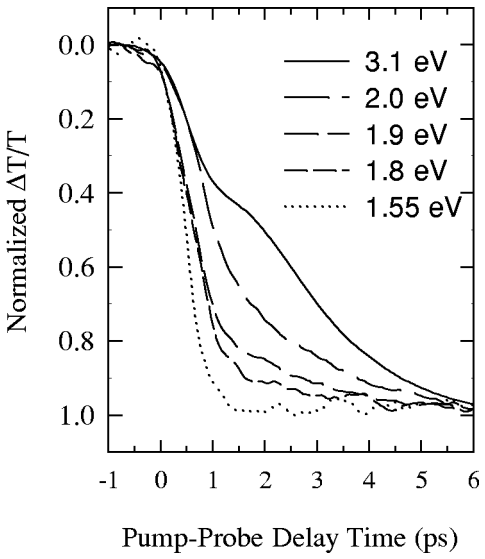

FIG. 3. One-dimensional pump scans of GaAs(100) at different pump photon energies. At higher pump photon energies, photoexcited electrons can access the satellite valleys which have a lower mobility (see Fig. 4). The absorption of THz radiation depends upon the carrier mobility. Thus the change in absorption can be used to measure scattering rates from the satellite valley back to the central Γ valley. (Ref. 33).

For GaAs the total measured $\Delta T/T$ is proportional to the absorption coefficient α, which is related to the mobility of the photoexcited electrons. The rise and fall times of the observed signal can be used to obtain dynamical information

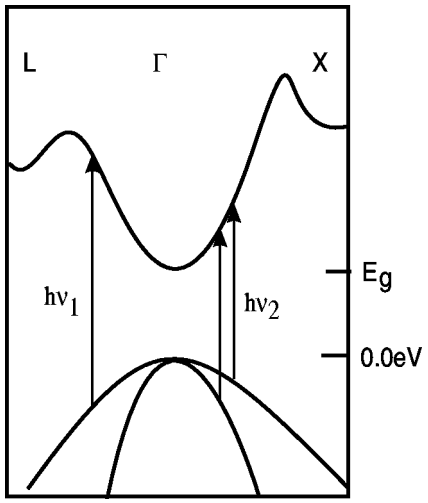

FIG. 4. GaAs band structure showing different possible excitation schemes. In excitation scheme 1, the optical photon excites carriers high enough in the Γ valley to allow scattering to the *L* or *X* valleys. In this case the onset of photoconductivity will be governed by the return of the electrons from the *L* or *X* into the Γ valley where the mobility is highest. Excitation scheme 2 excites the electron directly into the Γ valley, and the dynamics will be due to relaxation solely in the Γ valley.

about relaxation and scattering rates. However, a 1D pump scan is not adequate when the photoresponse includes a change in index of refraction, or when the transient absorption has a frequency dependence. In these cases, an observed change in $\Delta T/T$ could be due to a transient distortion of the THz pulse or a change in index of refraction, and not related to the average THz absorption by free carriers. Only a complete 2D data set will obtain all the dynamical information available in a TRTS experiment.

The analysis of the 2D data set is more difficult than treating each scan as a conventional static time-domain-THz (TD-THz) difference scan. In such static TH_z-TDS experiments the power spectrum and phase of the reference is compared with that of a photoexcited scan to extract the change in optical density (ΔOD) and change in phase ($\Delta\phi$). These values are then used to calculate the absorption coefficient α and index of refraction n.[49]

Two related issues occur in a TRTS experiment that complicate this simple analysis. First, at early pump-probe delay times the visible excitation pulse arrives at the sample as the THz pulse is propagating through it. The visible pulse affects only the trailing part of the THz pulse; therefore, the THz pulse experiences a different set of propagation parameters at the trailing end of the pulse than it did at the beginning. Second, the response of the material to photoexcitation, as described by its response function, is itself time dependent and will evolve during the THz propagation.

Figure 5 illustrates these effects. The figure is a contour plot of the THz difference scans [$\Delta E_{\mathrm{THz}}(t,t'')$ is equal to pump on minus pump off] as a function of pump-probe delay, t''. A line is drawn at 45° to the t'' axis and everything below and to the left of the line is a result of the THz arriving before the visible pulse, while everything to the right and above the line is obtained when the THz arrives after the visible pulse. Several THz transients are shown in Figs. 5(a)–5(d). The arrows represent the arrival of the visible pulse, and correspond to the arrows on the 2D grid. It is apparent that the THz difference scans of Figs. 5(a)–5(c) can not be thought of as static TH_z-TDS experiments.

The change in response function in GaAs is proportional to the change in conductivity, $\Delta\sigma(t,t'')$. The measured difference signal ΔE will be a convolution of the change in response function and the input THz pulse. These complications were formally discussed in the context of photoexcitation in liquids, and the results can be applied to transient photoconductivity with only minor modifications.[50] Therein, Kindt and Schmuttenmaer showed that scanning delay 1 (THz transmitter) in reverse, with delays 2 (THz receiver) and 3 (pump delay) fixed is equivalent to synchronously scanning delays 2 and 3 together with delay 1 fixed. Either scenario results in every portion of measured THz transient experiencing the same delay from the visible pulse.

Collecting the data synchronously is equivalent to a numerical projection of the 2D data set shown in Fig. 5 along the constant $u=t-t''$ axis, and the result is shown in Fig. 6(a). The change in response function can now be described by $\Delta\sigma(t,u)$. Since u is constant, $\Delta\sigma$ only depends parametrically on pump-probe delay time, $\Delta\sigma(t;t'')$, and therefore represents the photoexcited optical properties at each t''. We collect the data conventionally and project out $\Delta E(t,u)$ numerically, because we must also deconvolve the

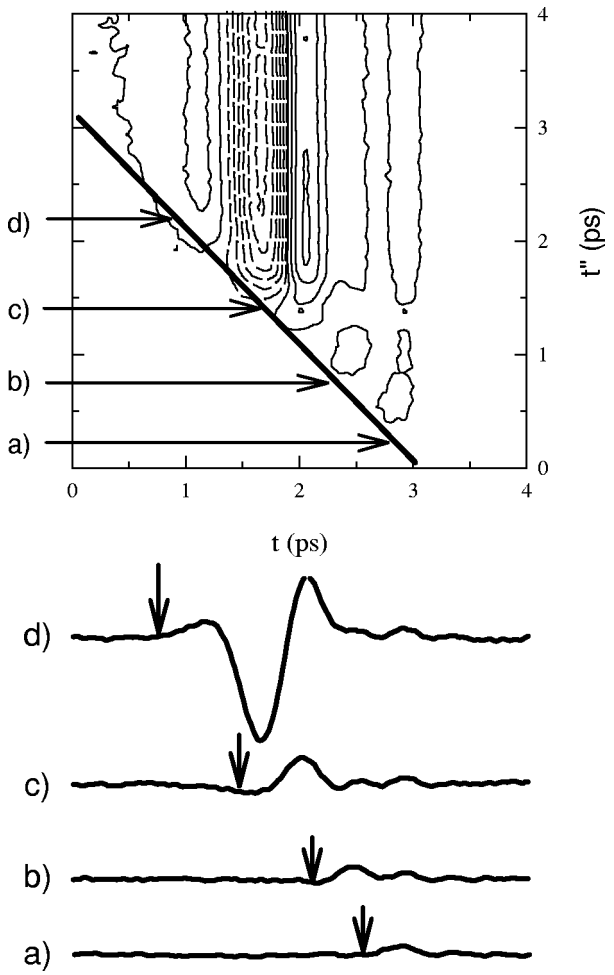

FIG. 5. Contour plot of two-dimensional (2D) raw THz difference scans collected by fixing the pump delay line while scanning the probe delay line. Solid lines correspond to positive values, while dashed lines correspond to negative values. The arrows labeled (a)–(d) represent different arrival times of the pump beam, and the corresponding difference scans are shown below the figure. (a) corresponds to the pump arriving after the main part of the THz but still affecting the trailing part. As the pump arrival time approaches the main feature of the THz pulse [(b) and (c)] a larger difference scan is measured, until pump delay time (d), which represents the pump coming well before the probe. The line at 45° represents the constant $u=t-t''$ axis.

detector response from the measured wave form as is discussed in Ref. 41. Once the data have been collected and deconvolved from the detector response as shown in Fig. 6(b), each pulse in the grid can be treated as an individual THz scan.

To extract the photoexcited optical constants (absorption coefficient α, and index of refraction n) we must consider the photoexcited path length d, and the reflectivity loses at the two interfaces (air/photoexcited GaAs and photoexcited GaAs/bulk GaAs). We obtain d by employing a model which includes diffusion, surface recombination, and bulk recombination effects, as discussed in Sec. III A. The reflectivity losses at the two surfaces are not known *a priori*. In addition, the spatial extent of the THz pulse is much larger than the path length traversed. Both the reflectivity changes and the

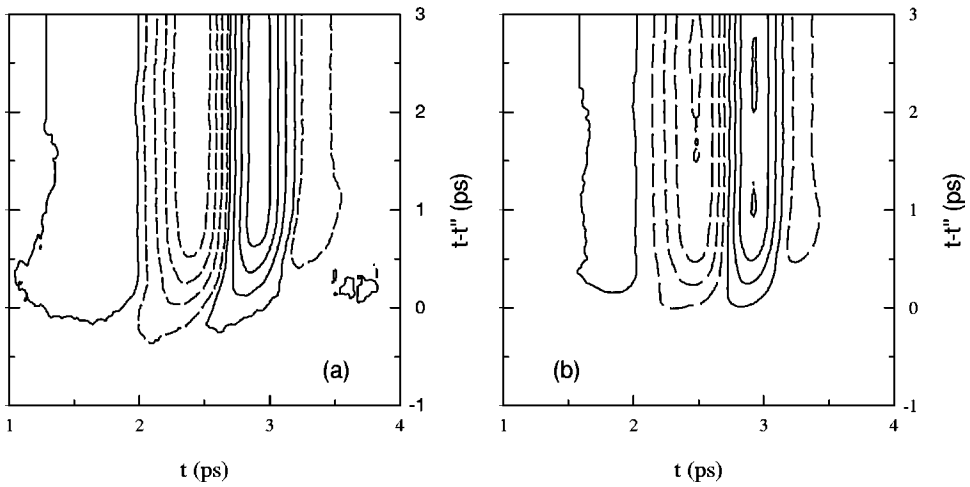

FIG. 6. Two-dimensional (2D) contour plot of $\Delta E(t,t-t'')$. Solid lines correspond to positive values, while dashed lines correspond to negative values. Plot (a) is the raw collected data after projection onto the constant $u=t-t''$ axis. Plot (b) is obtained after the detector response has been deconvolved, and the data projected onto the constant $u=t-t''$ axis. Plot (a) shows features appearing prior to the pump pulse arrival due to the finite detector response. Plot (b) shows that these features have essentially been removed.

small path length lead to an effect where the THz pulse appears to propagate with superluminal velocities in photoexcited GaAs. Schall and Jepsen accounted for this behavior by considering the small path length and front surface interface only.[40] However, to be most quantitative we have found that inclusion of *both* interfaces is needed. To do so we have used thin-film transmission formulas derivable in the frequency domain from Maxwell's equations.[51] We also find that the ''superluminal'' propagation is entirely accounted for when employing the thin-film formulas (and also in our numerical propagation described in Sec. III C).

A detailed description of the procedure used to obtain $\alpha(\omega)$ and $n(\omega)$ can be found in Ref. 41. The complex permittivity, ε, is determined from α and n using $\varepsilon'=n^2-k^2$ and $\varepsilon''=2nk$, where $k=\alpha c/(2\omega)$. The complex conductivity is obtained through

$$\varepsilon=\varepsilon_{\mathrm{GaAs}}-\frac{i\sigma}{\varepsilon_0\omega}, \tag{2}$$

where $\varepsilon_{\mathrm{GaAs}}=(n_{\mathrm{GaAs}})^2$, and ε_0 is the permittivity of free space.

III. RESULTS AND DISCUSSION

To fully characterize the photoconductivity in GaAs, a wide range of experiments were performed. The conditions used in these experiments are listed in Table I. In each case the photon energy was kept to within 100 meV of the band edge to avoid intervalley scattering. Therefore, the data are not affected by velocity overshoot because the carriers cannot access the satellite valleys. Consequently, we probe the change in mobility solely in the Γ valley (Fig. 4). We have

TABLE I. Experimental parameters. Columns A—M list the experimental conditions for the different 2D pump-probe experiments. λ is the wavelength of the photoexcitation pulse in nm, $\mathrm{KE}_{e,\mathrm{HH}}$ and $\mathrm{KE}_{e,\mathrm{LH}}$ are the kinetic energies in meV of electrons excited from the heavy- and light-hole bands, respectively, and n_{HH} and n_{LH} are the number of $\hbar\omega_{\mathrm{LO}}$ above the conduction-band minimum for electrons excited from the heavy- and light-hole bands, respectively. The bandwidth of the visible excitation pulse is given in meV, and the pulse width in femtoseconds is the FWHM of the excitation pulse. The optical skin depth of the absorption in GaAs is given in μm, (Ref. 54), and the nascent photoexcited carrier density is *N*. Data with parameters from column *F* are shown as representative data sets in Figs. 10–12.

	Temperature 75 K [a]									Temperature 300 K [b]			
	A	B	C	D	E	F	G	H	I	J	K	L	M
λ (nm)	808	809	803.5	799	793	789	783	778	774	803.6	799	795	786.6
$\mathrm{KE}_{e,\mathrm{HH}}$ (meV)	28.3	26.9	36.6	45.4	55.4	64.3	73.5	83.5	91	109	117	124	140
$\mathrm{KE}_{e,\mathrm{LH}}$ (meV)	14.8	13.9	18.9	23.4	28.3	32.3	37.7	42.5	46.5	55.7	59.6	63.2	71.1
n_{HH}	0.78	0.75	1.01	1.26	1.54	1.78	2.04	2.3	2.5	3.0	3.25	3.44	3.88
n_{LH}	0.13	0.39	0.53	0.65	0.79	0.90	1.0	1.2	1.3	1.5	1.66	1.76	1.98
Bandwidth (meV)	10.4	11.7	11.6	11.8	13.7	13.0	13.0	12.0	11.5	17	20	19	18
Pulse width (fs)	280	100	280	280	280	280	280	280	280	100	100	100	100
Skin depth (μm)	1.1	0.99	0.94	0.90	0.86	0.82	0.79	0.75	0.72	0.68	0.66	0.64	0.60
N ($\times 10^{16}$ cm^{-3})	1.8	0.1	0.4	2.2	2.3	2.1	2.4	2.5	2.6	2.0	8.6	5.0	6.1

[a] $E_g=1.504$ eV.
[b] $E_g=1.43$ eV.

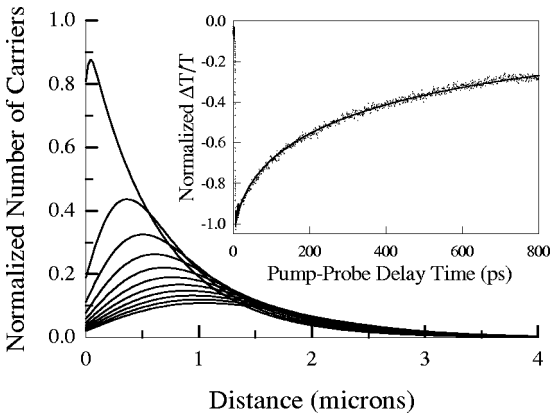

FIG. 7. The distribution of carriers as a function of distance into the sample, calculated from a diffusion model (Ref. 52) which includes terms for both bulk and surface recombination. Solid curves are profiles of the distribution at 50-ps intervals, starting 1 ps after photoexcitation. At $t=0$, the distribution is exponential. The inset is a room-temperature 1D pump scan of 800-ps duration (dots), which is fit to the calculated carrier density as a function of time after photoexcitation.

maintained the highest temporal resolution by deconvolving the detector response and numerically tracking the pump and probe beam delay lines together. This eliminates any artifacts from monitoring a mobility that is changing on a time scale which is faster than the THz pulse duration.

Our results are presented in four sections. Section III A discusses the 1D pump results (scanning the pump with fixed probe delay time). We determine the bulk and surface recombination dynamics from these studies. Section III B presents the 1D probe results (scanning the probe with fixed pump delay times). We show the accuracy of the TRTS method by comparing the measured data to that predicted by the Drude model. In Secs. III C and III D we discuss the early times where simple 1D probe and 1D pump scans are insufficient and 2D scanning is required. Section III C introduces the finite-difference time-domain (FDTD) method which is used to model the data, and Sec. III D compares the measured data to the FDTD simulations.

A. Bulk and surface recombination dynamics (1D pump)

The carrier recombination dynamics of photoexcited GaAs can be monitored with 1D TRTS experiments in which the change in THz transmission is measured as a function of the pump-probe delay time (see Sec. II B). While 1D pump scans are of limited use at short pump-probe delay times (<3 ps), when a change in index of refraction accompanies a change in absorption, this is not an issue at longer pump-probe delay times (>3 ps). The inset of Fig. 7 displays an 800-ps duration, room-temperature, 1D pump scan with a photoexcitation arclength of 790 nm. This scan illustrates that the recombination dynamics cannot be described by a single exponential, as would be expected from a single bulk recombination process. Instead, the data are fit to a calculated carrier density as a function of time after photoexcitation, which is extracted from the solution of a diffusion equation with terms for bulk recombination and the optical penetration depth of the visible excitation pulse.[52]

The diffusion equation is solved by the Laplace transform method utilizing boundary conditions that allow for carrier recombination at the surface. The diffusion equation used is[52]

$$\frac{\partial n}{\partial t}=D\frac{\partial^2 n}{\partial x^2}-\frac{n}{\tau_b}+\delta(t)\exp(-\alpha x), \tag{3}$$

where n is the number of carriers at a distance x into the sample, D is the diffusion coefficient in cm^2/s, τ_b is the bulk carrier lifetime in seconds, and α is the power absorption coefficient in cm^{-1} of the visible radiation with a δ function temporal profile. The diffusivity is obtained through the Einstein relation as

$$D=\frac{\mu_{\mathrm{ab}}k_B T}{|e|}, \tag{4}$$

where k_B is Boltzmann's constant, T is the temperature in K, and e is the charge of an electron in Coulombs. The ambipolar mobility μ_{ab} in $\mathrm{cm}^2\,\mathrm{V}^{-1}\,\mathrm{s}^{-1}$ is related to the electron and hole mobilities by

$$\frac{1}{\mu_{\mathrm{ab}}}=\frac{1}{\mu_e}+\frac{1}{\mu_h}. \tag{5}$$

The boundary conditions are

$$n(0,t)=\left.\frac{D\partial n(x,t)}{s\quad\partial t}\right|_{x=0} \tag{6a}$$

$$n(l,t)=0 \tag{6b}$$

$$n(x,0)=0, \tag{6c}$$

where s is the surface recombination velocity in cm/s, and l is an arbitrarily long distance into the sample at which the carrier density is zero for all time t after photoexcitation. The resulting carrier distribution as a function of distance into the sample and time after photoexcitation with a $\delta(t)$ pulse is $n(x,t)=\varphi(t,x)\exp(-t/\tau_b)$,[52] where

$$\varphi(t,x)=\exp\left(-\frac{x^2}{4Dt}\right)\left\{\frac{1}{2}\left[\omega\left(\alpha\sqrt{Dt}-\frac{x}{2\sqrt{Dt}}\right)+\frac{\alpha D+s}{\alpha D-s}\omega\left(\alpha\sqrt{Dt}+\frac{x}{2\sqrt{Dt}}\right)\right]-\frac{s}{\alpha D-s}\omega\left(s\sqrt{\frac{t}{D}}+\frac{x}{2\sqrt{Dt}}\right)\right\} \tag{7}$$

and ω is the exponentially scaled complementary error function, $\omega(z)=\exp(z^2)[1-\mathrm{erf}(z)]$. Since the measured change in THz transmission is proportional to the number of free carriers, we fit our 1D pump data to the total carrier concentration as a function of time after photoexcitation, $n(t)=\varphi^*(t)\exp(-t/\tau_b)$, where

$$\varphi^*(t)=\int_0^\infty \varphi(t,x)dx=\frac{s}{\alpha(s-\alpha D)}\omega(\alpha\sqrt{Dt})$$
$$-\frac{D}{s-\alpha D}\omega\left(s\sqrt{\frac{t}{D}}\right). \quad (8)$$

Figure 7 shows the calculated carrier distribution $n(x)$ at 50-ps intervals, starting 1 ps after photoexcitation. The values for τ_b and s used to calculate the carrier distributions shown are taken from the best fit to the data in the inset of Fig. 7. Literature values for the ambipolar mobility[53] ($\mu_{ab}=388\ \mathrm{cm^2\,V^{-1}\,s^{-1}}$) and absorption coefficient[54] ($\alpha=1620\ \mathrm{cm^{-1}}$) were used to obtain values for τ_b and s of 2.1 ns and 8.5×10^5 cm/s, respectively. Since the initial distribution of carriers at $t=0$ is an exponential distribution of the form $\exp(-\alpha x)$, the majority of the carriers are near the surface at early times, and surface recombination is the dominant relaxation process. It can be seen that at long delay times, as the carriers simultaneously diffuse into the bulk of the sample and recombine at the surface, bulk recombination becomes the dominant relaxation process. This accounts for the observed double-exponential behavior, and allows us to extract rates for both bulk and surface recombination processes.

The distributions calculated from this model are used to obtain d, which is used in the calculation of α and n as described elsewhere.[41] For a simple exponential distribution the path length is the $1/e$ point, or, equivalently, the total integral of the distribution. For more general distributions, involving the effects of surface recombination, one can obtain the path length in an analogous fashion by scaling the maximum of each distribution to unity and integrating to obtain d.

B. Mobility at long delay times (1D probe)

We have performed 1D probe scans at pump-probe delay times of 5, 10, 50, 100, 250, and 500 ps at both 300 and 77 K, where for each delay time the carriers have thermalized and relaxed within the central Γ valley. At such long times after photoexcitation, the Drude model is expected to describe the photoexcited optical properties. We have fit the data to a variety of models described below, and find that our results are best represented by a generalized form of the Drude model. Electron mobilities extracted from this treatment of the data are in good agreement with literature values.

The simplest model of electrical conductivity is the Drude model, which treats conduction electrons as free to move under the influence of an applied electric field but subject to a collisional damping force.[55] The frequency-dependent complex conductivity, $\sigma(\omega)$, is related to the dielectric susceptibility through $\sigma(\omega)=-i\omega\chi(\omega)$. The inverse Fourier transform of $\chi(\omega)$ yields the time domain response function, $\chi(t)$, and describes the evolution of the system after applying an electric field.[56] Drude theory assumes an exponential evolution with a relaxation time of τ. In the frequency domain the equation for the Drude conductivity is equivalent to the permittivity of a liquid based on Debye theory.[57] The Drude model can be modified in an analagous fashion as the ''Cole-Cole''[58] (CC) or ''Cole-Davidson''[59] (CD) models for liquids. The CC and CD (Ref. 60) theories both describe response functions with nonexponential relaxations, for example, the CD response function has the form[61]

$$\chi(t)=\frac{1}{\tau\Gamma(\beta)}\left(\frac{t}{\tau}\right)^{\beta-1}e^{-t/\tau}, \quad (9)$$

where $\Gamma(\beta)$ is the γ function with argument β, and τ is known as the critical relaxation time since there is actually a distribution of relaxation times. The CC response function has a similar form in that there is an $e^{-t/\tau}$ term, but it can not be written as a closed expression.[61] These nonexponential responses lead to a continuous distribution of relaxation times, and because of the large range of relaxation times involved, it is easier to work with a logarithmic distribution. In the case of the Drude model, the continuous distribution simply reduces to a δ function, $G(\ln\tau')=\delta(\tau-\tau')$. The CC model has a symmetric logarithmic distribution function, centered at $\ln\tau$, whose width increases with α, and becomes a δ function when $\alpha=0$.[61] The CD model has an asymmetric (actually one-sided) logarithmic distribution function that peaks at τ, and is zero for all times greater than τ. It falls off for values less than τ, falling off more slowly with smaller values of β, and reduces to a δ function at τ when $\beta=1$.[61] Both the CC and CD forms describe a response which is initially faster than the Drude form (with the CD model being faster than the CC model). Symmetric and asymmetric distributions of relaxation times can be included simultaneously to form (GD) generalized Drude model.

One of the main assumptions of the Drude model is the free-electron approximation (FEA). The FEA assumes that the electrons do not interact with the scatterers. Thus the scattering event is independent of the electron energy. The FEA accounts for most of the failure of the Drude model.[55] Inclusion of interactions with the scatterers leads to a ''memory effect,'' wherein the momentum and energy of the scattered electron depend on the incoming momentum and energy. The distribution of relaxation times described by the CC, CD, and GD models implies memory effect.[56,62] Photoconduction in GaAs does not strictly adhere to the FEA, and the response is better described by including a distribution of relaxation processes in the form of the GD model. This is hardly surprising, since we expect many different scattering processes in GaAs. For example, scattering occurs from LO phonons, heavy holes, impurities, and accoustic phonons, to name a few. Hill and Dissado[62] showed that even a simple case of two different Debye-type relaxation processes results in a nonexponential behavior of the response function, $\chi(t)$.

Jeon and Grischkowdky observed a deviation from the Drude model, and modified it to include energy-dependent relaxation from lattice impurity and acoustic phonon scattering events with $\tau^{-1}(E)=\tau_i^{-1}(E/k_BT_0)^{-3/2}+\tau_l^{-1}(E/k_BT_0)^{1/2}$, where $\tau^{-1}(E)$ is the overall scattering rate, τ_i^{-1} is the impurity scattering rate, τ_l^{-1} is the lattice (acoustic phonon) scattering rate, and T_0 is an additional fitting parameter with units of temperature.[63] Those scattering events did not account for their measured data, whereas a CD model did. We too have employed this scattering model, and find that it is not as good as the GD model. Invoking the

GD model to fit our data assumes that the true relaxation process is the average of a distribution of relaxation times, which are energy dependent.

The frequency-dependent complex conductivity is described by the GD model as

$$\sigma(\omega)=\frac{\varepsilon_0\omega_p^2\tau}{(1-(i\omega\tau)^{1-a})^{\beta}}, \tag{10}$$

where $\varepsilon_{\bigcirc}$ is the free-space permittivity, τ is the carrier collision time, and ω_p is the plasmon frequency. The plasmon frequency is defined as

$$\omega_p^2=Ne^2/(\varepsilon_0 m^*), \tag{11}$$

where N is the carrier density, e is the electron charge, and m^* is the effective mass of the electron in GaAs $(0.067m_e)$.[53] Electron mobilities can be calculated according to $\mu=e/(m^*\gamma)$, where the carrier damping rate $\gamma=1/\tau$. Equation (10) reduces to the CC model when $\beta=1$, the CD model when $\alpha=0$, and the Drude model when $\alpha=0$ and $\beta=1$.

Fits obtained using CC, CD, and GD models indicate that the CC model fits well to the real conductivity at frequencies below 1.2 THz, and that it fits well to the imaginary conductivity at frequencies above 0.9 THz. The CD model converges to the Drude model for these data ($\beta=1$), and thus need not be considered further. The Drude model fits well to the real conductivity at frequencies above 1.2 THz, but overestimates the imaginary conductivity for frequencies below 0.9 THz. Either model (CC or Drude) individually deviates from the data by as much as 20%, but when combined in the GD model reproduce the data to within +/- 3% for all frequencies less than 1.6 THz. Other THz spectroscopic studies on doped silicon found that the frequency-dependent conductivity fit well to the CD model,[57,63] and studies on doped GaAs found that the conductivity fit to the Drude model.[49] We performed pump-probe studies on silicon, and found that the conductivity fit better to the CC model, which indicates that the GD behavior we observe for GaAs may be due to the difference between photoexcited and doped conduction electrons.

Several additional modifications to the Drude model were investigated. The Drude conductivity was modified to allow the carriers to have two different damping rates, which allows for there to be two types of scattering processes. The model was then modified to allow for the existence of surface and bulk electrons, each with their own characteristic plasmon frequency and damping rate. Finally, the model was modified to include both electrons and holes as charge carriers. None of these models performed nearly as well as the GD model.

Based on these extensive comparisons, the GD model was chosen as the best theory to represent the measured data at long pump-probe delay times (>3 ps). Figure 8 displays the real and imaginary components of the frequency-dependent conductivity 100 ps after photoexcitation at 77 and 300 K. The GD fit reproduces the data well, and produces reasonable values for the electron mobility and carrier density. The 300-K electron mobility obtained from the fit is $\mu_e=6540$ cm^2 V^{-1} s^{-1} with a carrier density, obtained from Eq. (11), of $N=1.6\times10^{16}$ cm^{-3}. This is slightly less than the literature value[53] of 8600 cm^2 V^{-1} s^{-1}. The data at 77 K leads to a much higher mobility of $\mu_e=13600$ cm^{2}V^{-1}s^{-1}, with a carrier density of $N=1.5\times10^{16}$ cm^{-3}. An increase in mobility at lower temperatures is expected due to the decreased number of scattering events. In addition, the carrier densities obtained from the fits are similar to those calculated based on the spot sizes and intensities of the pump beam ($N=7.1\times10^{15}$ cm^{-3} at 300 K and $N=1.4\times10^{16}$ cm^{-3} at 77 K).

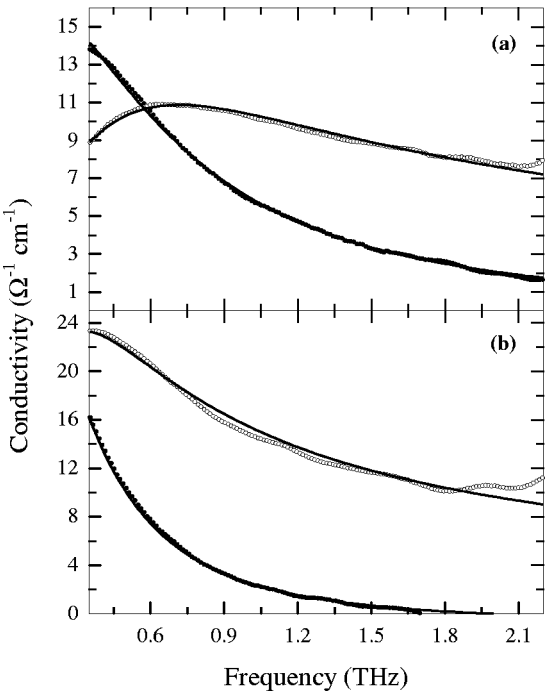

FIG. 8. Real (black circles) and imaginary (white circles) conductivity at 300 K (a) and 77 K (b), measured 100 ps after photoexcitation in GaAs in the ⟨100⟩ orientation. The fit (solid line) is the generalized Drude (GD) model.

The CC parameter α obtained from fits to the data at a variety of pump-probe delay times was found not to depend significantly on carrier concentration or pump-probe delay time. The CD parameter, β, was always greater than 0.8 and found to converge to 1 in the limit of low carrier concentrations. These trends are different than those observed by Jeon *et al.*[63] They found that the CD term converged to 1 at high carrier concentrations. Surface effects are an unlikely source of this discrepancy, because α was found not to depend on the amount of time after photoexcitation (at long times the carriers are far away from the surface). The most likely explanation for this is that our sample is photoexcited, not doped. In a doped sample carriers are continuously trapped and released from the ionic cores, whereas in a photoexcited sample, once an electron recombines with a hole it will not be released.

The calculated mobilities at 77 K as a function of carrier density are shown in Fig. 9. The mobility increases as the carrier concentration decreases, and is shown to fit well to the empirical Caughey-Thomas relation.[63,64]

C. TRTS finite-difference time-domain (FDTD) simulations

In an effort to better understand our results, we have numerically propagated THz pulses through a 0.7-μm-thick

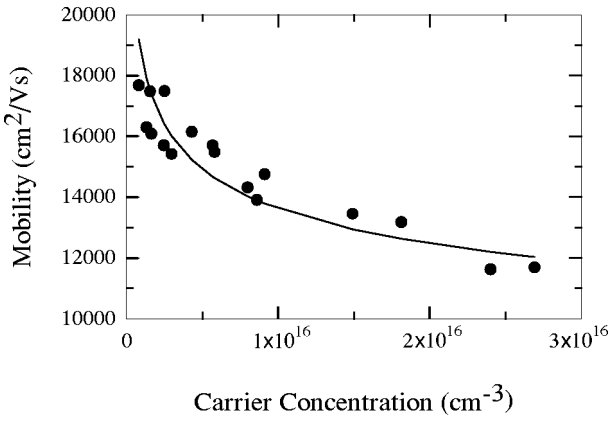

FIG. 9. Mobility at 77 K as a function of carrier concentration N as determined from the generalized Drude (GD) model. The mobility follows the empirical Caughey-Thomas curve (line). At lower concentrations the mobility is expected to level off again.

layer of photoexcited GaAs, bounded on one side by air, and the other by nonphotoexcited GaAs. The properties were changed from insulating to conducting as a function of time (using the Drude model with a time-dependent scattering rate) by simulating a Gaussian photoexcitation pulse. We find that the simulations reproduce the general trends seen in the data as will be discussed in Sec. III D.

The FDTD method was used with absorbing boundary conditions.[65–67] In this method, Maxwell's equations are solved numerically. We need only solve a 1D propagation problem since the radial dimension of the THz spot (2 mm) is much larger than the optical absorption depth of 0.7 μm. The magnetic and electric fields are obtained using[65]

$$H(s,t,t'')=H(s,t-dt,t'')-\frac{\Delta t}{\mu_0 \Delta s}[E(s+ds/2,t-dt/2,t'') - E(s-ds/2,t-dt/2,t'')] \tag{12}$$

and

$$D(s,t,t'')=D(s,t-dt,t'')-\frac{\Delta t}{\Delta s}[H(s+ds/2,t-dt/2,t'') - H(s-ds/2,t-dt/2,t'')], \tag{13}$$

where

$$D(s,t,t'')=\varepsilon_0 \varepsilon E(s,t,t'')+\varepsilon_0 \int_0^t E(t-\tau)\chi(\tau,t'')d\tau, \tag{14}$$

B is the magnetic field and $B=\mu_0 H$, μ_0 is the permeability of free space, E is the electric field, D is the electric displacement, s is the spatial position, and Δs is its step size. The propagation time is t, with step size Δt, and the pump-probe delay time is t''. The dielectric constant is $\varepsilon=\varepsilon_0 \varepsilon_\infty$, and $\chi(t',t'')$ is the dielectric response of the material. The above FDTD formalism is correct to second order. We have found a spatial step size of 0.025 μm is needed to adequately simulate a photoexcitation depth of 0.7 μm, and the temporal step size is 0.05 fs, much smaller than the Courant stability criterion.[68]

The time-domain dielectric response for photoexcited carriers in the Drude model is given by the solution of the Drude equation of motion,

$$\ddot{s}(t)=-\gamma \dot{s}(t)+\frac{e}{m_*}E(t), \tag{15}$$

where γ is the damping constant and m_* is the effective mass of the carrier. The solution is[66]

$$\chi(t',t'')=\frac{\omega_p^2(t'')}{\gamma(t'')}\{1-\exp[-\gamma(t'')t']\}, \tag{16}$$

where $\omega_p^2(t'')=e^2N(t'')/\varepsilon_0 m^*$ is the plasmon frequency, which depends on the time since the arrival of the pump pulse through the number of photoexcited electrons N that it generates. The damping constant $\gamma(t'')$ can also depend on time to simulate a time-dependent mobility. The above exponential form of the dielectric response leads to a simplification in the descritization of the FDTD formulas, and we have followed the procedure of Ref. 66.

We have compared an exponential distribution of carriers to a slab distribution using the FDTD method. We find that, for distributions with skin depths less than 3 μm, the error of assuming a slab distribution is less than 5% for carrier concentrations of $<10^{17}$ cm^{-3}. For skin depths larger than 3 μm, the error grows linearly with skin depth. However, we find that an exact solution can be obtained by dividing the distribution into small slices and expressing the transmission coefficient in terms of multiple layer formulas.[69] Furthermore, we investigated the effects of carrier profiles, such as those described in Sec. III A, where the surface recombination has depleted the carriers near the surface resulting in carrier distributions which are neither exponential nor slab. We find that these distributions behave more like the slab than the exponential. In fact, assuming a slab distribution introduces no additional error in obtaining the correct results, even for skin depths greater than 3 μm. As a result, we assume a slab distribution with path lengths determined, as discussed in Sec. III A.

D. Behavior at early times (2D pump probe)

One of the motivations for these studies was the desire to observe the dramatic changes predicted in the time-resolved, frequency-dependent conductivity for initial electron kinetic energies that are integer multiples of the LO-phonon frequency ($\hbar\omega_{\mathrm{LO}}$).[30] The excitation bandwidth was reduced to 6 nm (11 meV) so that the spread in kinetic energies was smaller than the LO-phonon energy (36 meV in GaAs). Photon energies were varied from less than $1\times\hbar\omega_{\mathrm{LO}}$ to almost $4\times\hbar\omega_{\mathrm{LO}}$ to investigate any trends in the data. Table I tabulates the different photon energies used, the relationship of the electron KE to $\hbar\omega_{\mathrm{LO}}$, the bandwidth of the pump laser, and the optical skin depth at each wavelength. We found that, for the most part, any differences as a function of electron kinetic energy were less than the reproducibility between data sets. Therefore, it is most productive to identify common characteristics among the data sets rather than differences.

Figures 10(a) and 10(c) and 11(a) and 11(c) show representative 2D plots of the real and imaginary parts of the

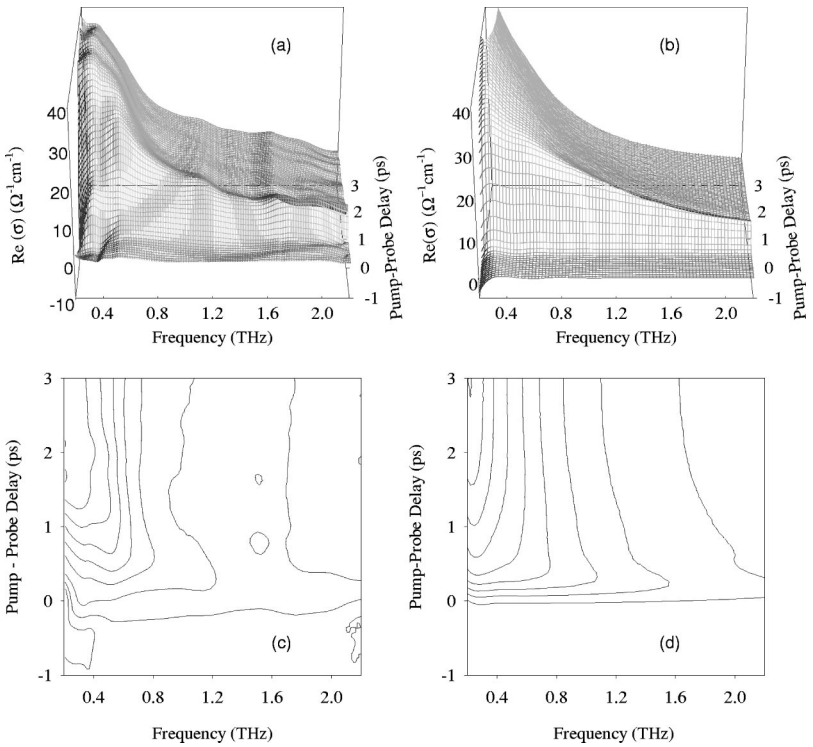

FIG. 10. Representative data set for the real part of the time-resolved, frequency-dependent conductivity. The data shown correspond to the experimental parameters given in Table I, column F. (a) is the measured data, (c) is a contour plot of (a), (b) is the FDTD simulated data, and (d) is a contour plot of (b). The simulation reproduces the data fairly well.

experimentally determined conductivity for GaAs. Figures 10(b) and 10(d) and 11(b) and 11(d) are the 2D plots of the simulated real and imaginary parts of the conductivity. The similarity between the actual data and the results of the simulation is quite good. To further quantify and understand the data, difference plots are shown in Figs. 12(a)–12(d). The difference plots were generated by subtracting a scaled long-time (3 ps) scan from entire data set. The long time scan was scaled with a sigmoid that increased from zero to one at time zero with a width equaling the width of the pump pulse. The difference plots show where the data deviates from its equilibrated values, and the main features of the deviation are not highly dependent on the width of the sigmoid.

The data can be divided into three regimes depending on the pump-probe delay time, and they are initial (-0.5–1 ps), intermediate (1–3 ps), and steady state (>3 ps). Several variations are observed as the conductivity evolves to its steady state (3 ps). The simulations do not completely reproduce the variations observed in the initial regime; however, they qualitatively reproduce the trends seen in all three re-

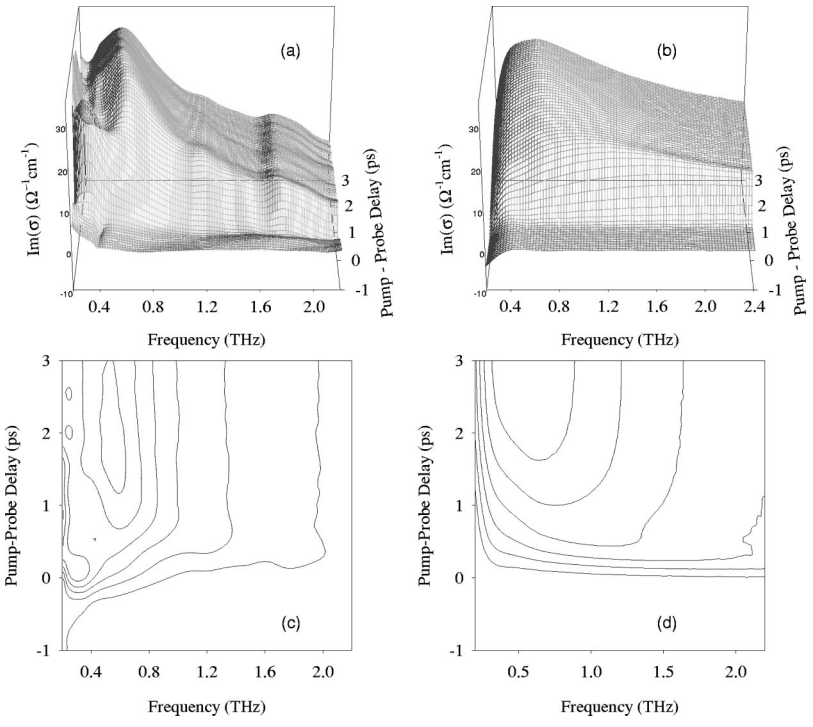

FIG. 11. Representative data set for the imaginary part of the time-resolved, frequency-dependent conductivity. The data shown correspond to the experimental parameters given in Table I, column F. (a) is the measured data, (c) is a contour plot of (a), (b) is the FDTD simulated data, and (d) is a contour plot of (b). Deviations of the data from the simulations are observed at low frequencies.

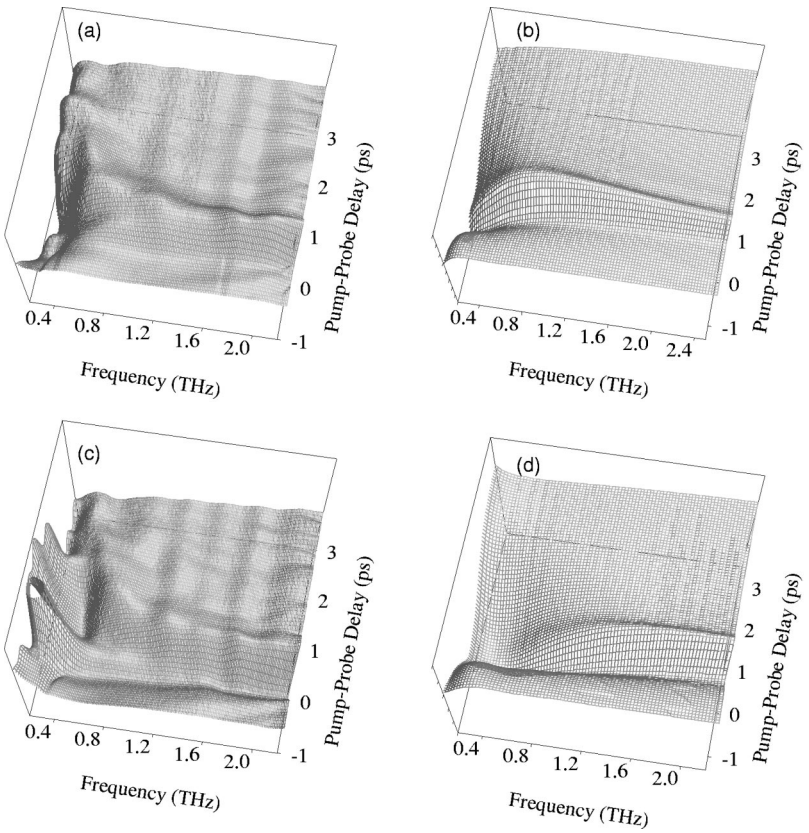

FIG. 12. Difference plots generated by subtracting a scaled long time (3 ps) 1D probe data set from the data. Difference plots are shown for the real (Re[σ]) (a) and imaginary (Im[σ]) (c) parts of measured conductivity. The difference plots for the FDTD simulated Re[σ] and Im[σ] are shown in (b) and (d), respectively. Deviations are most pronounced in Im[σ] at low frequencies, but both the Re[σ] and the Im[σ] contain deviations from 0 – 2.5 ps.

gimes, with the last two being reproduced best. The mobility initially increases rapidly, then decreases, and finally increases gradually to the steady-state value.

Initially, the conductivity is seen to rise simultaneously for all frequencies. Then the lower frequencies continue to rise while the higher frequencies decrease. A peak at low frequencies is observed in the imaginary part of the conductivity (Im[σ]) that is not reproduced in the simulations (see Figs. 10–12). This peak also causes the low frequencies in the Im(σ) to grow in faster than the high frequencies. The fact that the low frequencies grow in faster than the higher frequencies suggest this is not a detector limitation. The Re[σ] is well reproduced by the simulations. These observations are partially explained by ballistic transport of electrons.

Ballistic transport occurs when no scattering centers are present and therefore $\gamma=0$ in Eq. (15). The conductivity response in the frequency domain would be purely imaginary, and scale as ω^{-1}. This might account for the rise in the imaginary part of the conductivity at low frequencies. To further investigate ballistic transport, we allowed γ to be time dependent. Specifically, we allowed γ to start near zero and then rise to its limiting steady-state value. We compared this to simulations where γ was held constant. We find that including ballistic electrons enhances the Im[σ] at low frequencies, but not to the extent observed in the data. We conclude that ballistic transport cannot fully account for the behavior observed in the data.

An instantaneous acceleration of the electrons from the applied electric field of the THz probe pulse can take place when the photoexcitation occurs at the same time that the THz field is in the sample. At long times, when the pump comes well before the probe, the electrons will experience a gradual increase in the field and will only be gently accelerated. At the earliest times, however, the pump creates conduction electrons while the THz field is present. Thus the electrons experience an electric field upon being created. The acceleration of the electrons by the field radiates an additional field, and this may account for the observed response. This effect, however, is present in the simulations, and therefore cannot explain the observed deviations. We have verified that this nonlinear interaction is linearly dependent on pump intensity and THz amplitude.[70]

The second regime of the data encompasses 1–3 ps. The data show a peak in the Im[σ] at about 0.8 THz, that shifts to about 0.5 THz over the next 1.5 ps. A time-dependent scattering rate was included in the FDTD simulations to investigate this regime. Based on work of Vengurlekar and Jha[26] the scattering rate was large initially, and decreased exponentially to its steady-state value. These simulations qualitatively reproduce the trends seen in the data. In particular, the peak in the Im[σ] shifts rapidly from low frequencies (in the initial regime) to high frequencies, then gradually back to low frequencies. The peak of Im[σ] is related to the scattering rate γ which in turn is inversely related to the mobility by $\mu=e/(m^*\gamma)$. A plot of the peak of Im[σ] for the average of five data sets is shown in Fig. 13. These observations are in the spirit with the predictions of Vengurlekar and Jha, who predicted a time-dependent mobility due to the dynamics of the photoconducting electrons with the hot phonons.

Furthermore, the mobility increases more than the observed shift in the peak of Im[σ] to lower frequencies because the electron effective mass is decreasing as their distribution evolves from the initial photoexcited distribution to a thermalized one. The time-dependent mobility is related to

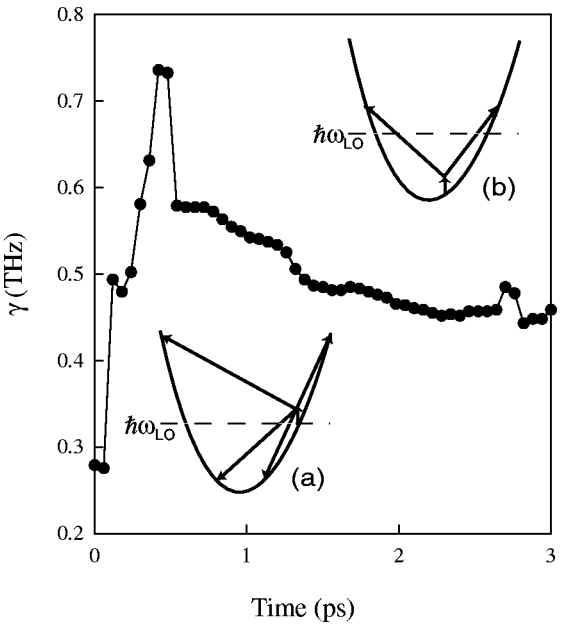

FIG. 13. Plot of the frequency at the peak of the imaginary part of the conductivity as a function of time after photoexcitation. This value corresponds to the scattering rate, γ. Variations as a function of time are attributed to phonon-assisted intravalley relaxation. Inset (a) shows far infrared (FIR) absorption assisted by LO-phonon absorption *and* emission. Inset (b) shows that after the electron distribution has relaxed below $\hbar\omega_{\mathrm{LO}}$, FIR absorption is only assisted by LO-phonon absorption.

the effective mass and the scattering rate by $\mu(t) = e/[\gamma(t)m^*(t)]$. The Γ valley of GaAs is slightly nonparabolic, and conduction electrons will have a different effective mass m^* depending on the distribution function of the photoexcited electrons, $f(E,t)$. The effective mass is obtained using Eq. (1). The effective mass is largest immediately following photoexcitation, and smallest at the band edge. The mobility increases as the distribution relaxes to the bottom of the Γ valley due to the decrease in both effective mass and scattering rate.

Two other potential explanations for the behavior between 1 and 3 ps, velocity overshoot and Coulombic screening, have been considered and ruled out. We have ruled out the possibility of velocity overshoot because of the low electron kinetic energies and low applied field. Even at the highest photon energies employed, the initial electron kinetic energy is 99 meV at 70 K and 117 meV at 300 K. As a worst case scenario, consider a Boltzmann distribution with the same kinetic energy as the photoexcited electrons, which would correspond to the carriers fully thermalizing among themselves prior to equilibration with the lattice. With this assumption, only about 5% of the carriers have kinetic energy above the *L*-valley minimum (300 meV). Therefore, the only way to transfer significant population into the *L* valley would be to apply a large electric field (the Gunn effect). However, the THz field (measured to be 110 V/cm at the sample) is much smaller than the required fields of about 3 kV/cm. Coulombic screening is also ruled out, because it does not become important until higher excitation densities and applied fields (5 kV/cm) are reached.[71] Therefore, we conclude that the observed dynamics are a result of the interactions between the photoexcited electrons and phonons.

Intraband free-carrier absorption is a phonon-mediated process. That is, to conserve both energy and momentum, the photon absorption must be accompanied by absorption or emission of a phonon (see the inset of Fig. 13). Thus the transient conductivity can depend on the phonon dynamics. The observed features exist over the range of times that are characteristic of electron-phonon coupling. For example, recent work has shown that as a high density of hot electrons cool, a large population of phonons can be created, which can then assist intraband absorption, and can also be reabsorbed by the electrons, thereby slowing the cooling rate.[72]

Since IR photon energies are much greater than the LO-phonon energy of 36 meV, intraband absorption typically occurs with either the absorption *or* emission of a phonon. Our situation is somewhat different because the FIR photon energy is less than the phonon energy. Specifically, as seen in the insets of Fig. 13, at early times phonons can be either absorbed or emitted to assist the photoabsorption, whereas at long delay times, after the carriers have relaxed to the bottom of the conduction band, the photon energy of absorption is not great enough to allow emission of a phonon to accompany photoabsorption. This effect is responsible for the decrease in γ at intermediate times.

In a series of papers, Vengurlekar and Jha detailed a theoretical prediction based on the Boltzmann transport equations for photoconducting electrons in GaAs.[26–30] Vengurlekar and Jha predicted a time-dependent mobility due to dynamics in the Γ valley as the electrons cool to the band edge by their interactions with the LO phonons through the Fröhlich interaction.[73] The momentum relaxation time τ_m will depend on electron-phonon dynamics because $\tau_m^{-1} = \tau_{\mathrm{LO}}^{-1} + \tau_1^{-1}$, where τ_{LO}^{-1} is the LO emission rate and τ_1^{-1} is the quasielastic scattering rate. At early times the photoexcited electrons can emit phonons, and $\tau_m \approx \tau_{\mathrm{LO}} \approx 150$ fs. After the electrons have cooled to below $\hbar\omega_{\mathrm{LO}}$, they can no longer emit LO phonons and $\tau_m \approx \tau_1 \approx 1-100$ ps. The quasielastic scattering rate describes scattering with the heavy holes, impurities, and acoustic phonons. Vengurlekar and Jha predicted that these dynamics occur on a time scale of 1–3 ps.[26] Our data verify these predictions. While the data reveal a time-dependent scattering rate, we do not observe a dramatic dependence on whether the photoexcited electrons are created with integer or half-integer multiples of $\hbar\omega_{\mathrm{LO}}$, as predicted.[30] Vengurlekar and Jha's predictions provide a description of the carrier mobility and scattering rates, but the scope of their work did not include calculation of intraband THz absorption. To do so would require explicit inclusion of the coupling of phonons in the intraband absorption process.

The last regime found in the data is the static, long-time limit. After 3 ps, the carriers have relaxed to the bottom of the conduction band. The mobility is seen to increase on a long time scale (>100 ps) as carriers disperse and relax, thereby lowering the overall carrier density.

IV. CONCLUSIONS

There are some important experimental considerations to be aware of when carrying out TRTS studies. In particular, it is necessary to project the data onto the constant $u = t - t''$ axis (either numerically or physically) before further analysis. It is also necessary to deconvolve the detector response

function if the sample response is faster than the detector response. The need for deconvolution becomes evident when there are features in the data that appear to arrive at negative time delays.

This paper demonstrates that TRTS can accurately measure the carrier dynamics and mobility in a photoexcited sample. We chose bulk GaAs as a prototypical benchmark system, and found good agreement with literature values at long pump-probe delay times, after the carriers have sufficiently thermalized.

Finally, this work uncovers a contribution to the frequency-dependent conductivity on time scales from 0.2 to 3 ps that has not been previously observed, to our knowledge. These results are in the spirit of the predictions from Vengurlekar and Jha [30] We attribute these features to the influence of phonon dynamics on intraband free-carrier absorption.

Future work will investigate the Boltzmann transport equations derived by Vengurlekar and Jha in order to understand the differences between the observed data and the theoretical predictions. In addition, we will extend this type of study to materials that are difficult to characterize with conventional methods, such as semiconductor quantum dots and dye-sensitized colloidal TiO_2.

ACKNOWLEDGMENTS

We would like to thank J. T. Kindt for providing early versions of the computer programs used for numerical pulse propagation. We would like to acknowledge financial support from the National Science Foundation CAREER Award program, and the Camille and Henry Dreyfus New Faculty Award Program.

[1] J. Shah, *Ultrafast Spectroscopy of Semiconductors and Semiconductor Nanostructures* (Springer, New York, 1996).
[2] A. Othonos, Appl. Phys. Rev. **83**, 1789 (1998).
[3] A. J. Taylor, D. J. Erskine, and C. L. Tang, J. Opt. Soc. Am. B **2**, 663 (1985).
[4] J. L. Oudar, A. Migus, D. Hulin, G. Grillon, J. Etchepare, and A. Antonetti, Phys. Rev. Lett. **53**, 384 (1984).
[5] P. C. Becker, H. L. Fragnito, C. H. B. Cruz, J. Shah, R. L. Fork, J. E. Cunningham, J. E. Henry, and C. V. Shank, Appl. Phys. Lett. **53**, 2089 (1988).
[6] C. J. Stanton and D. W. Bailey, Phys. Rev. B **47**, 1624 (1993).
[7] M. Ulman, D. W. Bailey, L. H. Acioli, F. G. Vallee, C. J. Stanton, E. P. Ippen, and J. G. Fujimoto, Phys. Rev. B **47**, 10 267 (1993).
[8] U. Hohenester, P. Supancic, P. Kocevar, X. Q. Zhou, W. Kutt, and H. Kurz, Phys. Rev. B **47**, 13 233 (1993).
[9] A. Leitenstorfer, C. Furst, A. Laubereau, W. Kaiser, G. Trankle, and G. Weimann, Phys. Rev. Lett. **76**, 1545 (1996).
[10] L. Min and R. J. D. Miller, Chem. Phys. Lett. **163**, 55 (1989).
[11] L. Min and R. J. D. Miller, Appl. Phys. Lett. **56**, 524 (1990).
[12] T. Elsaesser, J. Shah, L. Rota, and P. Lugli, Phys. Rev. Lett. **66**, 1757 (1991).
[13] D. W. Snoke, W. W. Ruhle, Y. C. Lu, and E. Bauser, Phys. Rev. Lett. **68**, 990 (1992).
[14] L. Rota, P. Lugli, T. Elsaesser, and J. Shah, Phys. Rev. B **47**, 4226 (1993).
[15] A. Leitenstorfer, A. Lohner, T. Elsaesser, S. Haas, F. Rossi, T. Kuhn, W. Klein, G. Boehm, G. Traenkle, and G. Weimann, Phys. Rev. Lett. **73**, 1687 (1994).
[16] M. U. Wehner, J. Hetzler, and M. Wegener, Phys. Rev. B **55**, 4031 (1997).
[17] S. Yu, J. Lee, and A. Viswanath, J. Appl. Phys. **86**, 3159 (1999).
[18] P. C. Becker, H. L. Fragnito, C. H. B. Cruz, R. L. Fork, J. E. Cunningham, J. E. Henry, and C. V. Shank, Phys. Rev. Lett. **61**, 1647 (1988).
[19] A. Lohner, K. Rick, P. Leisching, A. Leitenstorfer, T. Elsaesser, T. Kuhn, F. Rossi, and W. Stolz, Phys. Rev. Lett. **71**, 77 (1993).
[20] C. J. Stanton and D. W. Bailey, Phys. Rev. B **45**, 8369 (1992).
[21] C. J. Stanton, D. W. Bailey, and K. Hess, Phys. Rev. Lett. **65**, 231 (1990).
[22] T. Kuhn and F. Rossi, Phys. Rev. Lett. **69**, 977 (1992).
[23] F. Rossi, S. Haas, and T. Kuhn, Phys. Rev. Lett. **72**, 152 (1994).
[24] F. Rossi, S. Haas, and T. Kuhn, Semicond. Sci. Technol. **9**, 411 (1994).
[25] R. Binder, D. Scott, A. E. Paul, M. Lindberg, K. Henneberger, and S. W. Koch, Phys. Rev. B **45**, 1107 (1992).
[26] A. S. Vengurlekar and S. S. Jha, J. Appl. Phys. **65**, 3189 (1989).
[27] A. S. Vengurlekar and S. S. Jha, Phys. Rev. B **41**, 1286 (1990).
[28] A. S. Vengurlekar and S. S. Jha, Appl. Phys. Lett. **51**, 323 (1987).
[29] A. S. Vengurlekar and S. S. Jha, Phys. Rev. B **38**, 2044 (1988).
[30] A. S. Vengurlekar and S. S. Jha, Phys. Rev. B **43**, 12 454 (1991).
[31] M. C. Nuss, D. H. Auston, and F. Capasso, Phys. Rev. Lett. **58**, 2355 (1987).
[32] B. I. Greene, P. N. Saeta, D. R. Dykaar, S. Schmitt-Rink, and S. L. Chuang, IEEE J. Quantum Electron. **28**, 2302 (1992).
[33] S. E. Ralph, Y. Chen, J. Woodall, and D. McInturff, Phys. Rev. B **54**, 5568 (1996).
[34] M. C. Nuss, in *Ultrafast Phenomena VI, Springer Series in Chemical Physics*, edited by T. Yajima, K. Yoshihara, C. B. Harris, and S. Shionoya (Springer-Verlag, New York, 1988), pp. 215–217.
[35] B. I. Greene, J. F. Federici, D. R. Dykaar, A. F. J. Levi, and L. Pfeiffer, Opt. Lett. **16**, 48 (1991).
[36] P. N. Saeta, J. F. Federici, B. I. Greene, and D. R. Dykaar, Appl. Phys. Lett. **60**, 1477 (1992).
[37] R. H. M. Groeneveld and D. Grischkowsky, J. Opt. Soc. Am. B **11**, 2502 (1994).
[38] S. S. Prabhu, S. E. Ralph, M. R. Melloch, and E. S. Harmon, Appl. Phys. Lett. **70**, 2419 (1997).
[39] B. N. Flanders, D. C. Arnett, and N. F. Scherer, IEEE J. Sel. Top. Quantum Electron. **4**, 353 (1998).
[40] M. Schall and P. U. Jepsen, Opt. Lett. **25**, 13 (2000).
[41] M. C. Beard, G. M. Turner, and C. A. Schmuttenmaer (unpublished).
[42] A. Rice, Y. Jin, X. F. Ma, X. C. Zhang, D. Bliss, J. Larkin, and M. Alexander, Appl. Phys. Lett. **64**, 1324 (1994).
[43] A. Nahata, A. S. Weling, and T. F. Heinz, Appl. Phys. Lett. **69**, 2321 (1996).
[44] Y. Cai, I. Brener, J. Lopata, J. Wynn, L. Pfeiffer, J. B. Stark, Q. Wu, X. C. Zhang, and J. F. Federici, Appl. Phys. Lett. **73**, 444 (1998).

[45] C. Winnewisser, P. U. Jepsen, M. Schall, V. Schyja, and H. Helm, Appl. Phys. Lett. **70**, 3069 (1997).
[46] Q. Wu, M. Litz, and X. C. Zhang, Appl. Phys. Lett. **68**, 2924 (1996).
[47] Q. Wu and X. C. Zhang, IEEE J. Sel. Top. Quantum Electron. **2**, 693 (1996).
[48] A. Yariv and P. Yeh, *Optical Waves in Crystals: Propagation and Control of Laser Radiation* (Wiley, New York, 1984).
[49] N. Katzenellenbogen and D. Grischkowsky, Appl. Phys. Lett. **61**, 840 (1992).
[50] J. T. Kindt and C. A. Schmuttenmaer, J. Chem. Phys. **110**, 8589 (1999).
[51] J. A. Stratton, *Electromagnetic Theory*, 1st ed. (McGraw-Hill, New York, 1941).
[52] J. Vaitkus, Phys. Status Solidi A **34**, 769 (1976).
[53] J. I. Pankove, *Optical Processes in Semiconductors* (Prentice-Hall, Englewood, NJ, 1971).
[54] M. Sturge, Phys. Rev. **127**, 768 (1962).
[55] N. Ashcroft and N. Mermin, *Solid State Physics* (Saunders College Publishing, New York, 1976).
[56] G. A. Niklasson, J. Appl. Phys. **62**, R1 (1987).
[57] T. I. Jeon and D. Grischkowsky, Appl. Phys. Lett. **72**, 2259 (1998).
[58] K. S. Cole and R. H. Cole, J. Chem. Phys. **9**, 341 (1941).
[59] D. W. Davidson and R. H. Cole, J. Chem. Phys. **19**, 1484 (1951).
[60] G. A. Niklasson, J. Phys.: Condens. Matter **5**, 4233 (1993).
[61] C. Böttcher and P. Bordewijk, *Theory of Electric Polarization*, 2nd ed. (Elsevier, New York, 1978), Vol. 2.
[62] R. M. Hill and L. A. Dissado, J. Phys. C **18**, 3829 (1985).
[63] T. I. Jeon and D. Grischkowsky, Phys. Rev. Lett. **78**, 1106 (1997).
[64] D. M. Caughey and R. E. Thomas, Proc. IEEE **50**, 2192 (1967).
[65] K. S. Yee, IEEE Trans. Antennas Propag. **AP-14**, 302 (1966).
[66] R. J. Luebbers, F. Hunsberger, and K. S. Kunz, IEEE Trans. Antennas Propag. **39**, 29 (1991).
[67] J. P. Berenger, J. Comput. Phys. **114**, 185 (1994).
[68] W. H. Press, S. A. Teukolsky, W. T. Vetterling, and B. P. Flannery, *Numerical Recipes in Fortran*, 2nd ed. (Cambridge University Press, New York, 1986).
[69] L. Brekhovskikh, *Waves in Layered Media*, *Applied Mathematics and Mechanics* (Academic Press, New York, 1960).
[70] D. J. Cook, J. X. Chen, E. A. Morlino, and R. M. Hochstrasser, Chem. Phys. Lett. **309**, 221 (1999).
[71] B. Hu, E. de Souza, W. Knox, J. Cunningham, and M. Nuss, Phys. Rev. Lett. **74**, 1689 (1995).
[72] H. P. M. Pellemans and P. C. M. Planken, Phys. Rev. B **57**, R4222 (1998).
[73] P. Yu and M. Cardona, *Fundamentals of Semiconductors* (Springer-Verlag, Berlin, 1996).